

# The Advantages of Polarization Control in RABBITT

Maria M. Popova and Elena V. Gryzlova

*Skobeltsyn Institute of Nuclear Physics, Lomonosov Moscow State University, 119991 Moscow, Russia and  
A.V. Gaponov-Grekhov Institute of Applied Physics,  
Russian Academy of Sciences, 603950 Nizhny Novgorod, Russia*

Sergei N. Yudin and Alexei N. Grum-Grzhimailo

*Skobeltsyn Institute of Nuclear Physics, Lomonosov Moscow State University, 119991 Moscow, Russia  
(Dated: October 29, 2024)*

The RABBITT setup is theoretically studied for various combinations of XUV and IR field components polarization: ‘linear+linear’, ‘linear+circular’ with crossed propagation directions, and ‘circular+circular’ with parallel propagation directions. The general properties of photoelectron angular distributions and their responses to the variation of the IR pulse delay are studied. Numerical simulations are performed for the neon valence shell ionization into the region of structureless continuum using two approaches based on time dependent perturbation theory and solution of rate equations. To distinguish between “geometrical” governed by fields’ polarization and spectroscopic features, additional analysis for the case of  $s$ -shell ionization is presented.

Since the very beginning of photoionization experiments, it has been well known that angle-resolved measurements provide more profound and detailed information about a process than measurements of the angle-integrated probabilities [1]. Application of a multicolor field significantly enhances experimental capabilities because the polarization and propagation directions of the field components can be modulated separately [2]. That paved a way to the measurements of different types of dichroism, primarily linear and circular magnetic dichroism. The first attempts to access dynamical peculiarities of multiphoton ionization were based on variation of the time offset (lag) between pump and probe fields [3, 4]. The development of highly coherent sources of extreme ultraviolet (XUV) and X-ray radiation, such as high-order harmonic generation (HHG) setups [5–7] or X-ray free electron lasers (XFELs) [8, 9], opens a fruitful perspective for the vector correlation control in the attosecond metrology. That has made possible experimental studying of the dynamics of small quantum systems on attosecond timescales [10–13].

Attosecond metrology based on the RABBITT (Reconstruction of Attosecond Beating By Interference of Two-photon Transitions) scheme [14], when an electron is promoted to the continuum by an XUV harmonic and then additionally absorbs or emits an optical (IR) photon, started with angle-integrated experiments [15–18] and appropriate theoretical considerations [19–21]. Meanwhile, the pathways’ interference that underlies the scheme manifests differently in different waves ( $s, p, d, \dots$ ) at the different photoemission angles [22]. The RABBITT experiments have advanced to the angle-resolved case [23–27], and different theoretical approaches have been applied [28]. Angle-resolved measurements provide more detailed information and allow for the separation different pathways [29–35]. Moreover, keeping in mind that energy dependency of vector correlations differs from that of angle-integrated one [36] and may be narrower and shifted, the investigation may be useful for resolving

overlapping resonances or in case when the XUV spectrum is very broad, causing single- and two-photon signals overlapping in energy.

The possibility to perform angle-resolved measurements is a milestone for schemes with a mixture of waves of different parities in a sideband: (a) XUV harmonics differ by  $3\omega$  [37–39], (b) a bichromatic combination  $\omega$  and  $2\omega$  is applied [24], and (c) significant quadrupole effects are expected.

In spite of great progress occurred in the field, very few investigations involving different harmonics’ polarizations (and their directions) are reported [28, 31, 40, 41]. As progress in the generation of circularly and elliptically polarized harmonics is essential [42–45], there is a need for a systematic investigation of polarization effects in the RABBITT setup. Special attention in such an investigation must be paid to angle-resolved observables. It is important to emphasize that for some combinations of the components’ polarizations and propagation directions, RABBITT oscillations may appear only in angle-resolved parameters, even in a conventional scheme with odd XUV components that differ by  $2\omega$ .

Unless otherwise specified, the atomic system of units is used.

## I. THEORETICAL BASEMENT FOR THE RABBITT DESCRIPTION

In the paper we extend the approaches based on the solving of rate equations and time dependent perturbation theory applied earlier for linearly polarized fields [46, 47] to the systems with more complex geometries (polarization and propagation direction of the field component). Thus, here we briefly describe the methods clearly indicating polarization aspects.

The electromagnetic field is presented as a sum of XUV

harmonics of an order  $N$  generated on a seed IR pulse:

$$\mathbf{E}(t) = \Re \left[ \sum_{N\Lambda\lambda} E_{\text{xuv}} c_{\Lambda} \epsilon_{\Lambda} e^{-i(N\omega t + \phi_N)} + E_{\text{ir}} c_{\lambda} \epsilon_{\lambda} e^{-i(\omega t + \phi)} \right], \quad (1)$$

where  $E_{\text{xuv}} = E_{\text{xuv}}^0 \cos^2(\frac{t}{\tau})$  and  $E_{\text{ir}} = E_{\text{ir}}^0 \cos^2(\frac{2t}{\tau})$  are slowly varying envelopes with  $E_{\text{ir}}^0$  and  $E_{\text{xuv}}^0$  being strengths of the IR and XUV components, respectively, and  $\tau$  determines the pulse duration;  $\phi_N$  is Nth XUV component phase, and  $\phi$  is the varying phase shift of the IR pulse connected with the conventional in such experiments IR pulse delay  $\tau_{\text{del}}$  as  $\phi = 2\omega\tau_{\text{del}}$ . We use cosine envelope instead of Gaussian one because it provides smoothness at the (finite) edges of the pulse. Polarization of the field is determined by decomposition over cyclic coordinate vectors  $\epsilon_{\lambda/\Lambda=0,\pm 1}$  with coefficients  $c_{\lambda/\Lambda}$ . The coefficients before  $\epsilon_{\lambda/\Lambda=0}$  appear when photon wave vector is not parallel to the quantization axis  $z$  (see Table 1 below).

The atomic Hamiltonian is presented in the form:

$$i \frac{\partial}{\partial t} \Psi(\mathbf{r}, t) = \left( \hat{H}_{\text{at}} + \hat{H}_{\text{int}}(t) \right) \Psi(\mathbf{r}, t), \quad (2)$$

where  $\hat{H}_{\text{at}}$  is unperturbed Hamiltonian and  $\hat{H}_{\text{int}}(t)$  describes the interaction with electromagnetic field in the dipole approximation and velocity gauge with electric field potential  $\mathbf{A}(t) = -c \int \mathbf{E}(t) dt$ .

In the  $LS$ -coupling scheme within the frozen core approximation, eigenfunctions of the system  $\psi_{\alpha_n}(\epsilon_n, \mathbf{r})$  depend on the following quantum numbers: energy  $\epsilon_n$  ( $\epsilon$  without an index if a state belongs to a continuum spectrum), core (ion) orbital momentum and spin  $L_c$  and  $S_c$ , active electron angular momentum  $l$  and spin  $s = 1/2$ , total angular momentum  $L$  and spin  $S$ , and their projections  $M_L = M$  and  $M_S$ . Accounting that the electric dipole operator does not change spin  $\Delta S = 0$  and an atom is initially in a state with a definite spin, we can rule out the spin quantum numbers for brevity:  $\psi_{\alpha_n}(\epsilon_n, \mathbf{r}) \equiv \psi_{(L_c l) L (S_c \frac{1}{2}) S M_L M_S}(\epsilon_n, \mathbf{r}) \equiv \psi_{(L_c l) LM}(\epsilon_n, \mathbf{r})$ . A wave function of the system  $\Psi(\mathbf{r}, t)$  is expanded in the basis of eigenfunctions of the unperturbed Hamiltonian:

$$\hat{H}_{\text{at}} \psi_{\alpha_n}(\epsilon_n, \mathbf{r}) = \epsilon_n \psi_{\alpha_n}(\epsilon_n, \mathbf{r}), \quad (3)$$

$$\Psi(\mathbf{r}, t) = \sum_{L_c l LM} \left( \sum_n \mathcal{U}_{(L_c l) LM}(\epsilon_n, t) \psi_{\alpha_n}(\epsilon_n, \mathbf{r}) e^{-i\epsilon_n t} + \int d\epsilon \mathcal{U}_{(L_c l) LM}(\epsilon, t) \psi_{\alpha_\epsilon}(\epsilon, \mathbf{r}) e^{-i\epsilon t} \right), \quad (4)$$

where  $\alpha_\epsilon$  means a set of quantum numbers of a state with an electron in continuum.

Then the system of differential equations for expansion coefficients:

$$\frac{d\mathcal{U}_{(L_c l) LM}(\epsilon_n', t)}{dt} = -i \sum_n \int e^{i(\epsilon_n' - \epsilon_n)t} \langle \psi_{\alpha_n'} | \hat{H}_{\text{int}}(t) | \psi_{\alpha_n} \rangle \mathcal{U}_{(L_c l) LM}(\epsilon_n, t) \quad (5)$$

is solved numerically in the *Rate Equations (RE)* method (for the continuum part  $\epsilon_n \rightarrow \epsilon$  and  $\psi_{\alpha_n} \rightarrow \psi_{\alpha_\epsilon}$ ). To describe the states of the continuum in (5), the discretization of continuum was applied, i.e. the integration was replaced by summation with even energy step  $d\epsilon = 10^{-3}$  a.u. Thereby  $|\mathcal{U}_{(L_c l) LM}(\epsilon_\epsilon, t)|^2$  is the probability to find an electron in the neighborhood  $d\epsilon$  of the energy value  $\epsilon$  at time  $t$ .

The decomposition of the vector potential into cyclic coordinates can be further decomposed into  $A_{\text{xuv}}(t)$  that describes XUV comb and  $A_{\text{ir}}^u(t)$  and  $A_{\text{ir}}^d(t)$  that describe IR and behave as  $e^{-i(\omega t + \phi)}$  and  $e^{i(\omega t + \phi)}$ , respectively. The component  $A_{\text{ir}}^u(t)$  is responsible for an absorption of an IR photon, and  $A_{\text{ir}}^d(t)$  — its emission.

Within the framework of *perturbation theory (PT)*, the coefficients  $\mathcal{U}_{(L_c l) LM}(\epsilon_n, t)$  in the equation (5) are in turn expanded into the series.

Henceforth, we specify a target as a shell of an unpolarized atom with initial orbital momentum  $L = 0$ .

The first order coefficients describe direct ionization to the main photolines (ML) by XUV components of the electric field:

$$\mathcal{U}_{(L_c l) LM}^{(1)}(\epsilon_f, t) = c_{\Lambda} \frac{1}{\sqrt{3}} (00, 1\Lambda | 1M) D_{(L_c l) 1}^{(1)}, \quad (6)$$

$$D_{(L_c l) 1}^{(1)} = -i \langle \epsilon_f; (L_c l) 1 | \hat{D} | \epsilon_0, 0 \rangle \int_{-\tau/2}^{\tau/2} A_{\text{xuv}}(t) e^{i(\epsilon_f - \epsilon_0)t} dt, \quad (7)$$

where  $(00, 1\Lambda | 1M)$  is equal to 1 for each  $\Lambda$  but it determines a specific  $M$ , and we suppose the component to be completely polarized that means that with appropriate choice of a coordinate system only one  $c_{\Lambda} \neq 0$ .

The second order amplitudes describe absorption (' $u$ ') or emission (' $d$ ') of an IR photon leading to appearance of sidebands (SB) by up- and down-energy transitions:

$$\mathcal{U}_{(L_c l) LM}^{(2), u/d}(\epsilon_f, t) = \frac{(\pm 1)^\lambda}{\sqrt{3} \hat{L}} \sum_{\lambda} c_{\lambda} (1\Lambda, 1 \pm \lambda | LM) D_{(L_c l) L}^{(2), u/d}, \quad (8)$$

$$D_{(L_c l) L}^{(2), u/d} = \sum_n \langle \epsilon_f, (L_c l) L | D | \epsilon_n, 1 \rangle \langle \epsilon_n, 1 | D | \epsilon_0, 0 \rangle \int_{-\tau}^{\tau} A_{\text{IR}}^{u/d}(t) e^{i(\epsilon_f - \epsilon_n)t} \int_{-\tau/2}^t A_{\text{xuv}}(t') e^{i(\epsilon_n - \epsilon_0)t'} dt' dt, \quad (9)$$

where '+' sign is for absorption amplitude, and '-' sign is for emission. Factor  $(\pm 1)^\lambda$  comes from taking complex conjugation in cyclic basis:  $\epsilon_{+1}^* = -\epsilon_{-1}$  and vice versa. In equation (8), conventional notation for Clebsch—Gordan coefficients is used and  $\hat{a} = \sqrt{2a + 1}$ .

The photoelectron angular distribution (PAD) in PT

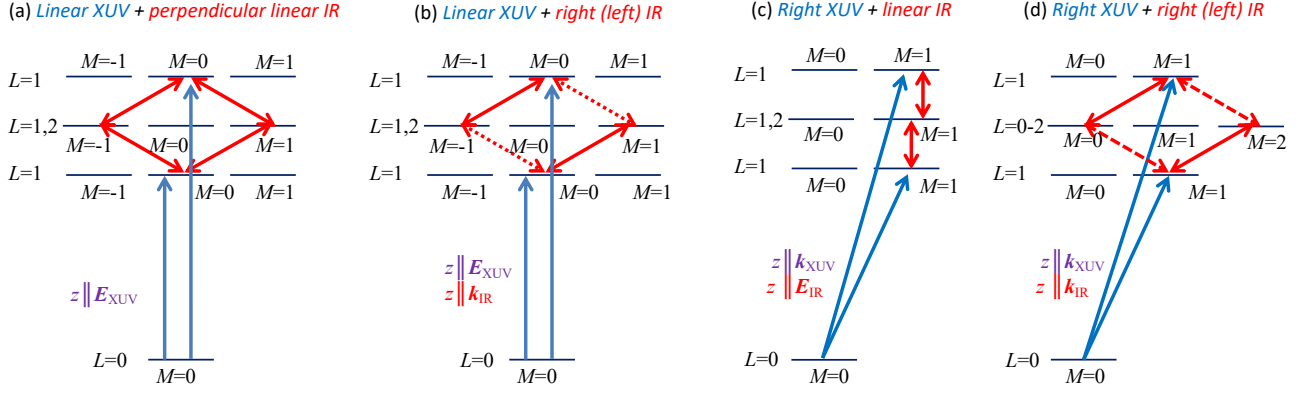


FIG. 1. The scheme of RABBITT for different geometries: (a) XUV and IR are linearly polarized in the orthogonal directions; (b) Circularly polarized IR and linearly polarized XUV harmonics; (c) Circularly polarized XUV and linearly polarized IR harmonics; (d) both IR and XUV harmonics are circularly polarized.

and RE is described as:

$$W(\varepsilon_f, t; \vartheta, \varphi) = \frac{1}{4\pi} \sum_{\substack{kqll'LL' \\ nn'\nu\nu'}} (-1)^{L_c+L+L'+k-M'} \hat{U}^{\nu} \hat{L} \hat{L}' \\ (l0, l'0 | k0)(LM, L' - M' | kq) \begin{Bmatrix} l & L & L_c \\ L' & l' & k \end{Bmatrix} \\ \mathcal{U}_{(L_c l)LM}^{(n), \nu}(\varepsilon_f, t) \mathcal{U}_{(L_c l')L'M'}^{(n'), \nu'*}(\varepsilon_f, t) \frac{\sqrt{4\pi}}{\hat{k}} Y_{kq}(\theta, \varphi), \quad (10)$$

where  $\nu$  is an order of amplitude in PT (in RE the resulting amplitude  $\mathcal{U}_{(L_c l)LM}(\varepsilon_f, t)$  is an ‘infinite sum’ over  $\nu$ ). In equation (10), conventional notations for Wigner  $6j$ -symbol and spherical harmonics are used.

In eq. (10), there are terms corresponding to the absorption ( $\mathcal{U}^{(2),u} \mathcal{U}^{(2),u*}$ ) and emission ( $\mathcal{U}^{(2),d} \mathcal{U}^{(2),d*}$ ) of IR photon which do not depend on the IR time-delay; and interference between absorption and emission amplitudes ( $\mathcal{U}^{(2),u} \mathcal{U}^{(2),d*}$ ) which depends on the IR delay and oscillates on the double IR frequency  $2\omega$ .

## II. THE PAD FOR DIFFERENT GEOMETRIES

In figure (1), there are schemes of RABBITT spectroscopy for the systems under consideration: (a) XUV and IR are linearly polarized in the orthogonal directions (quantization axis is along the XUV component polarization  $z \parallel \mathbf{E}_{\text{XUV}}$ ); (b) Circularly polarized IR and linearly polarized ( $\mathbf{E}_{\text{XUV}} \parallel \mathbf{k}_{\text{IR}}$ ) XUV (quantization axis is along the XUV component polarization  $z \parallel \mathbf{E}_{\text{XUV}}$ ); (c) Circularly polarized XUV and linearly polarized IR ( $\mathbf{E}_{\text{IR}} \parallel \mathbf{k}_{\text{XUV}}$ ) harmonics (quantization axis is along the IR component polarization  $z \parallel \mathbf{E}_{\text{IR}}$ ); (d) both IR and XUV harmonics are circularly polarized (quantization axis is along the field propagation direction  $z \parallel \mathbf{k}_{\text{IR}} \parallel \mathbf{k}_{\text{XUV}}$ ).

The case of the linearly polarized in the same direction XUV and IR fields we studied earlier in [47]. The quantum numbers in figure (1) are depicted for a system

TABLE I. The polarization coefficients  $c_\lambda$  (1) in the cyclic basis  $\{-, 0, +\}$  for different geometries and the list of allowed channels.

geometries system	(a) $z \parallel \mathbf{E}_{\text{XUV}}$	(b) $z \parallel \mathbf{E}_{\text{XUV}}$	(c) $z \parallel \mathbf{k}_{\text{XUV}}$	(d) $z \parallel \mathbf{k}_{\text{XUV}}$
$c_{\text{XUV}}$	$\{0, 1, 0\}$	$\{0, 1, 0\}$	$\{0, 0, 1\}$	$\{0, 0, 1\}$
$c_{\text{IR}}$	$\{\frac{e^{i\gamma}}{\sqrt{2}}, 0, -\frac{e^{-i\gamma}}{\sqrt{2}}\}$	$\{0, 0, 1\}$	$\{0, 1, 0\}$	$\{0/1, 0, 1/0\}$
Helium-like	$\varepsilon d^{u,d}$	$\varepsilon d^{u,d}$	$\varepsilon d^{u,d}$	$\varepsilon d^{u,d}, \varepsilon s^d$
Noble gases	$\varepsilon p^1 P^{u,d}$ $\varepsilon p^1 D^{u,d}$ $\varepsilon f^1 D^{u,d}$	$\varepsilon p^1 P^{u,d}$ $\varepsilon p^1 D^{u,d}$ $\varepsilon f^1 D^{u,d}$	$\varepsilon p^1 P^{u,d}$ $\varepsilon p^1 D^{u,d}$ $\varepsilon f^1 D^{u,d}$	$\varepsilon p^1 S^u$ $\varepsilon p^1 P^u$ $\varepsilon p^1 D^{u,d}$ $\varepsilon f^1 D^{u,d}$

\*: the index ( $u$ ) marks the channels proceeding with absorption of the IR photon, ( $d$ ) with emission.

with initial orbital momentum  $L = 0$  (a noble gas). Further we apply the approach to valence shell ionization of Neon and specify the general equations for the  $s$ -shell ionization ( $1s$  of He,  $2s$  of Ne,  $3s$  of Ar etc).

In table I, channels allowed for the different geometries under consideration are presented. For the (a)–(c) geometries, final projection of magnetic quantum number  $M = 1$ , therefore, the terms are  $P$  ( $L = 1$ ) and  $D$  ( $L = 2$ ). For the helium-like systems, there is a single  $d$ -wave channel because parity conservation rule prohibits emission of  $\varepsilon p$ -wave. The (d) geometry is exceptional because the  $S$ , ( $L = 0$ ) (for neon) and  $\varepsilon s$  (for helium) channel is involved for down-energy (equal helicities of IR and XUV) or up-energy (opposite helicities) transitions.

### A. A shell of a noble gas

It is convenient to extract a fields’ polarization-independent dynamical parameter  $B_k^{(\nu\mu)}[L, L']$  from the general angular distribution equation (10). For the side-

bands in the second order of PT it takes a form:

$$B_k^{(\mu\mu')}[L, L'] = \frac{(-1)^{L_f+L+L'}}{12\pi} \sum_{ll'} \hat{l}l'(l0, l'0 | k0) \quad (11)$$

$$\left\{ \begin{matrix} L & L' & k \\ l' & l & L_f \end{matrix} \right\} D_{(Lcl)L}^{(2),\mu} D_{(Lcl)L}^{(2),\mu'*},$$

where  $\mu, \mu' = u, d$ , and the dynamical parameters obey permutation equation  $B_k^{(\mu\mu')}[L, L'] = B_k^{(\mu'\mu)}[L', L]^*$ . In the case of the RE, the definition (11) is fair, except that instead of the second-order term  $D_{(Lcl)L}^{(2),\mu}$  one must consider a complete amplitude that possesses given quantum numbers.

Now the angular distributions for specific geometries can be written down in an easier for an analysis form:

$$W(\theta, \varphi)^{(a)} = \sum_{kLL'} \frac{(-1)^{L+L'+1}}{2} (B_k^{(dd)}[L, L'] + B_k^{(uu)}[L, L'] + B_k^{(ud)}[L, L'] + B_k^{(du)}[L, L'])$$

$$((L1, L' - 1 | k0)P_k(\cos\theta) + (-1)^{L'}(L1, L'1 | k2) \frac{\sqrt{4\pi}}{\hat{k}} (\eta Y_{k2}(\theta, \varphi) + \eta^* Y_{k-2}(\theta, \varphi))) \quad (12)$$

$$= \frac{\sigma^{(a)}}{4\pi} \left( 1 + \sum_{k=2,4} \beta_k^{(a)} P_k(\cos\theta) + \beta_{k2}^{(a)} \frac{\sqrt{4\pi}}{\hat{k}} (\eta Y_{k2}(\theta, \varphi) + \eta^* Y_{k-2}(\theta, \varphi)) \right); \quad (13)$$

$$W(\theta, \varphi)^{(b)} = \sum_{kLL'} \frac{(-1)^{L+L'+1}}{2} (L1, L' - 1 | k0) (B_k^{(dd)}[L, L'] + B_k^{(uu)}[L, L']) P_k(\cos\theta) \quad (14)$$

$$+ (L1, L'1 | k2) \frac{(-1)^L}{2} \frac{\sqrt{4\pi}}{\hat{k}} (B_k^{(ud)}[L, L'] Y_{k2}(\theta, \varphi) + B_k^{(du)}[L', L] Y_{k-2}(\theta, \varphi))$$

$$= \frac{\sigma^{(b)}}{4\pi} \left( 1 + \sum_{k=2,4} \beta_k^{(b)} P_k(\cos\theta) + \frac{\sqrt{4\pi}}{\hat{k}} (\beta_{k2}^{(b)} Y_{k2}(\theta, \varphi) + \beta_{k2}^{(b)*} Y_{k-2}(\theta, \varphi)) \right); \quad (15)$$

$$W(\theta, \varphi)^{(c)} = \sum_{kLL'} (L1, L' - 1 | k0) \frac{-1}{2} (B_k^{(dd)}[L, L'] + B_k^{(uu)}[L, L'] + B_k^{(ud)}[L, L'] + B_k^{(du)}[L', L]) P_k(\cos\theta); \quad (16)$$

$$= \frac{\sigma^{(c)}}{4\pi} \left( 1 + \sum_{k=2,4} \beta_k^{(c)} P_k(\cos\theta) \right) \quad (17)$$

$$W(\theta, \varphi)^{(d)} = \sum_{kLL'} ((L0, L'0 | k0)(11, 1 - 1 | L0)(11, 1 - 1 | L'0) B_k^{(dd)}[L, L'] + (22, 2 - 2 | k0) B_k^{(uu)}[2, 2]) P_k(\cos\theta)$$

$$- (22, L'0 | k2)(11, 1 - 1 | L'0) \frac{\sqrt{4\pi}}{\hat{k}} (B_k^{(ud)}[2, L'] Y_{k2}(\theta, \varphi) + B_k^{(du)}[L', 2] Y_{k-2}(\theta, \varphi)) \quad (18)$$

$$= \frac{\sigma^{(d)}}{4\pi} \left( 1 + \sum_{k=2,4} \beta_k^{(d)} P_k(\cos\theta) + \frac{\sqrt{4\pi}}{\hat{k}} (\beta_{k2}^{(d)} Y_{k2}(\theta, \varphi) + \beta_{k2}^{(d)*} Y_{k-2}(\theta, \varphi)) \right). \quad (19)$$

The parameter  $\eta = -\exp[-2i\gamma]/2$  is defined by the angle  $\gamma$  of IR polarization vector with respect to the  $x$ -axis in the  $xy$ -plane. Equations (13), (15), (17) and (19) themselves are the definition of the integral photoemission probability  $\sigma^{a,b,c,d}$  and angular anisotropy parameters  $\beta_{kq}^{a,b,c,d}$ . The parameters  $\beta_{22(42)}$  are defined to be in consistency with conventional parameters  $\beta_{2(4)}$  ( $\frac{\sqrt{4\pi}}{\hat{k}} Y_{k0}(\theta, \varphi)$  is a Legendre polynomial  $P_k(\cos\theta)$ ). The angular anisotropy parameters  $\beta_{kq}$  allow us characterize the angular distributions by a few numbers (see Fig. 3).

The following general conclusions can be drawn about the properties of the angle-integrated probabilities and PADs:

1. For the (a)- and (c)-geometry, the IR phase  $\phi$  affects both the overall probability for an electron to be emitted at a given energy ( $\sigma = \sigma(\phi)$ ) and the angular anisotropy parameters ( $\beta = \beta(\phi)$ ); all of the angular anisotropy parameters are real; PAD inherits the symmetries of the resulting field: for case (a) three orthogonal symmetry planes (see fig. 2a) and for case (c) axial symmetry with respect to the IR polarization vector accompanied with orthogonal symmetry plane (see fig. 2c).
2. For the (b)- and (d)-geometries, the phase-averaged part of eqs. (14) and (18) which contains  $B^{dd}$  and  $B^{uu}$  is axially symmetrical, while the inter-

ference term contains  $B^{ud}$  and  $B^{du}$  that depend on azimuth angle  $\varphi$ ; as a result, a complete PAD possesses the only one symmetry plane orthogonal to the IR propagation direction. Neither angle-averaged spectrum nor the PAD changes with variation of the IR phase  $\phi$  except for the rotation of the last around  $z$ -axis: eqs. (15) and (19) incorporating  $\beta_{22,42}$  depend on IR phase as  $\exp[\pm 2i(\phi - \varphi)]$ . The angular anisotropy parameters  $\beta_{2(4),2}$  caused by interference are complex.

3. The circular magnetic dichroism can be observed only for the (d)-geometry.
4. The angular anisotropy parameters being a ratio of harmonic functions of  $\phi$  are periodical but not

harmonic functions of IR phase  $\phi$ .

## B. Helium-like system

In this paragraph we consider additional features which arise when the ionized shell is a  $s$ -shell, so called *helium-like system*. In this case, the number of allowed ionization channels reduces significantly and they are characterized only with photoelectron angular momentum  $l$ . For (a)–(c) geometries, there is only one allowed channel: ionization to  $d$ -wave, for (d)-geometry, there are two channels:  $d$ - and  $s$ -waves (see table I). Equation (10) for the sidebands turns into an extremely simple form:

$$W(\theta, \varphi)^{(a)} = \frac{1}{8\pi} (|D_{\varepsilon d}^u|^2 + |D_{\varepsilon d}^d|^2 + D_{\varepsilon d}^u D_{\varepsilon d}^{d*} + D_{\varepsilon d}^d D_{\varepsilon d}^{u*}) \sin^2 \theta \cos^2 \theta \cos^2(\varphi - \phi - \gamma) \quad (20)$$

$$W(\theta, \varphi)^{(b)} = \frac{1}{16\pi} (|D_{\varepsilon d}^u|^2 + |D_{\varepsilon d}^d|^2 + e^{2i\varphi} D_{\varepsilon d}^u D_{\varepsilon d}^{d*} + e^{-2i\varphi} D_{\varepsilon d}^d D_{\varepsilon d}^{u*}) \cos^2 \theta \sin^2 \theta. \quad (21)$$

$$W(\theta, \varphi)^{(c)} = \frac{1}{16\pi} (|D_{\varepsilon d}^u|^2 + |D_{\varepsilon d}^d|^2 + D_{\varepsilon d}^u D_{\varepsilon d}^{d*} + D_{\varepsilon d}^d D_{\varepsilon d}^{u*}) \cos^2 \theta \sin^2 \theta; \quad (22)$$

$$W(\theta, \varphi)^{(d)} = \frac{1}{12\pi} \sum_{kl'l'} (l0, l'0 | k0)^2 (11, 1-1 | l0)(11, 1-1 | l'0) D_{\varepsilon l}^d D_{\varepsilon l'}^{d*} P_k(\cos \theta) + \frac{1}{32\pi} |D_{\varepsilon d}^u|^2 \sin^4 \theta - \frac{1}{12\pi} \sum_{kl'l'} (20, l'0 | k0)(22, l'0 | k2)(11, 1-1 | l'0) \frac{\sqrt{4\pi}}{\hat{k}} (D_{\varepsilon d}^u D_{\varepsilon l'}^{d*} Y_{k2}(\theta, \varphi) + D_{\varepsilon d}^{d*} D_{\varepsilon l}^d Y_{k-2}(\theta, \varphi)). \quad (23)$$

Here  $D_{\varepsilon l}^{u/d} \equiv D_{(0l)l}^{(2),u/d}$ . In figure 2, the general pattern of PAD for helium-like system is presented. For the (a) and (c)-geometries they are unconditional, for (b) plotted under assumption that  $D_{\varepsilon d}^u = D_{\varepsilon d}^d$ .

In the case of helium-like system one may conclude the following:

1. For the (a) and (c)-geometries, only  $d$ -wave left, and absorption and emission amplitudes come into the equations equally. The PADs turn into completely geometrical form with  $\beta_2^{(a),(c)} = 5/7$ ,  $\beta_4^{(a),(c)} = -12/7$ ,  $\beta_{22}^{(a)} = -5\sqrt{6}/7$ , and  $\beta_{42}^{(a)} = -6\sqrt{10}/7$ .
2. For the (b)-geometry,  $d$ -wave absorption ( $u$ ) and emission ( $d$ ) amplitudes contribute to PAD differently, and the PAD is partly geometrical:  $\beta_2^{(b)} = 5/7$ ,  $\beta_4^{(b)} = -12/7$ ,

$$\beta_{22}^{(b)} = \frac{5\sqrt{6} D_{\varepsilon d}^u D_{\varepsilon d}^{d*}}{7(|D_{\varepsilon d}^u|^2 + |D_{\varepsilon d}^d|^2)} \quad \beta_{42}^{(b)} = \frac{6\sqrt{10} D_{\varepsilon d}^u D_{\varepsilon d}^{d*}}{7(|D_{\varepsilon d}^u|^2 + |D_{\varepsilon d}^d|^2)}.$$

3. For (a)–(c) geometries, the maximal probability of electron emission is observed at the polar angle  $\theta = \pi/4$ .

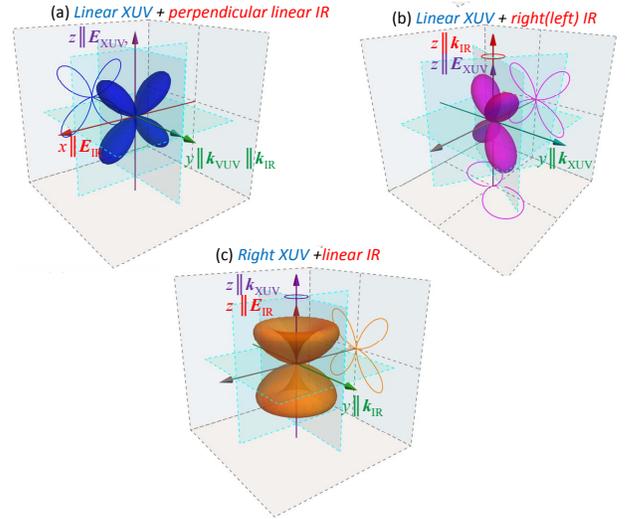


FIG. 2. The sample of PAD for the case of helium-like system and different geometries.

4. For (c)- and (d)-geometries, PAD possesses the same symmetries as in the general case. For (a)- and (b)-geometries, two additional symmetry planes arise: for (a) they are defined by the geome-

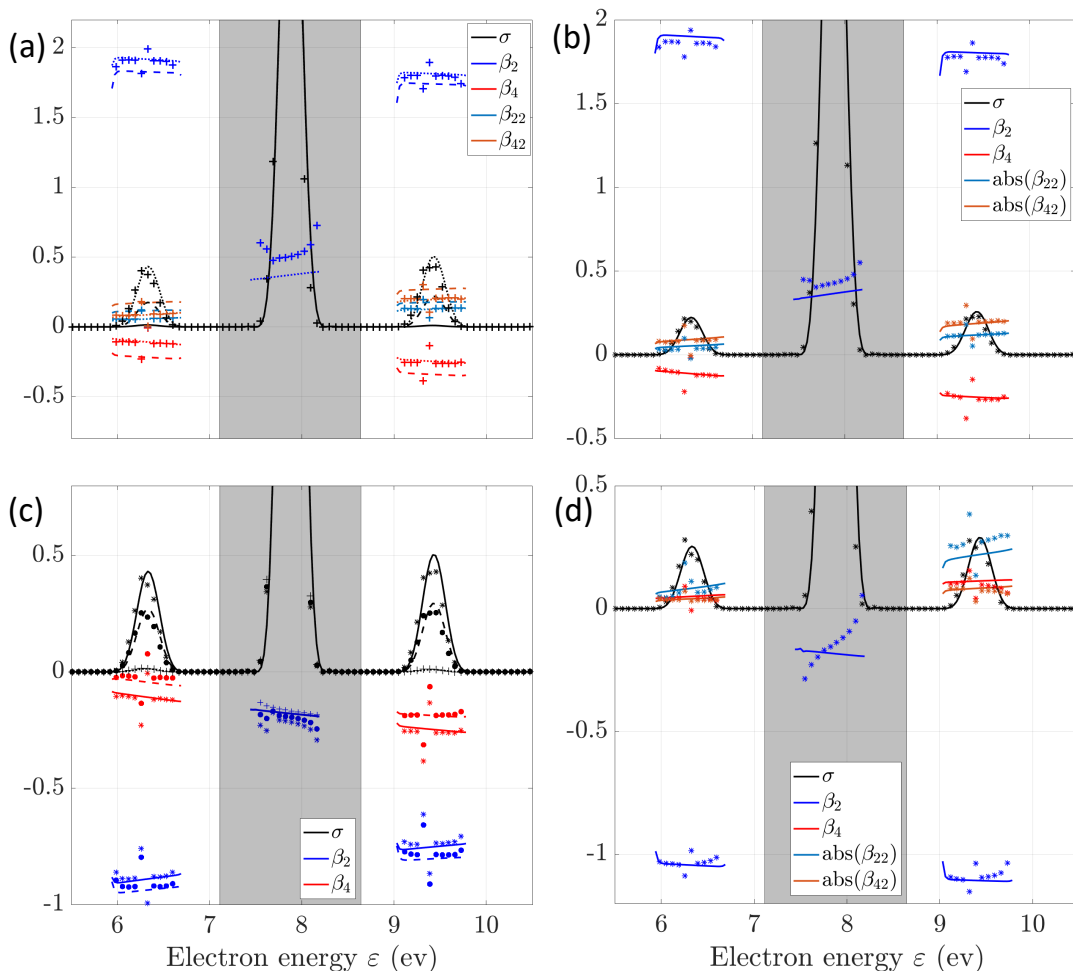


FIG. 3. Spectra (in arbitrary units) and angular anisotropy parameters as defined in eqs. (12)–(18) for geometries (a)–(d), respectively. Colors indicate a specific parameter (see the legends), and line type — IR phase and a model (solid lines are for PT and  $\phi = 0$ , stars are for RE and  $\phi = 0$ ; dashed lines and circles are for PT and RE for  $\phi = \pi/4$ , respectively; dotted lines and crosses are for PT and RE for  $\phi = \pi/2$ ).

try and make angle  $\pm\pi/4$  with polarization vectors of IR and XUV comb; for (b) they defined by phase between up- and down-pathways ( $\text{Arg}[D_{\varepsilon d}^u D_{\varepsilon d}^{d*}]$ ).

- For the (d)-geometry, there is a difference between pathways with the absorption and emission of an IR photon. While the first one leads to  $d$ -wave only, the second allows also  $s$ -wave. Therefore, the absorption pathway contributes to the plane orthogonal to the fields' propagation direction, and the emission pathway may contribute in the fields' propagation direction.

A short comment should be given about *circular dichroism* in the scheme (d). In this geometry, there is an essential difference in the allowed channels for the case when IR and XUV components have the same helicity compared to when they have opposite helicity. In the first case, pathways with IR absorption lead to  $L = 2$  ( $\varepsilon d$  for helium), while those with emission lead to  $L = 0, 1, 2$  ( $\varepsilon s(\varepsilon d)$  for helium). In the second case, the situation is

opposite. One can easily cast the equation for dichroism using (18) and (23). The interesting feature is that contribution of fourth-rank terms are strictly canceled in the dichroism for any target. It could be important for experimenters because extraction of higher rank anisotropy parameters are usually more difficult than those of 2nd rank.

Nevertheless for the region of smooth continuum chosen for numerical calculations in the next section, the difference in probabilities of up- and down-channels is little, and dichroism is not significant. One should look for a system with a sharp spectroscopic feature (autoionizing resonance) to observe the circular magnetic dichroism in a such setup.

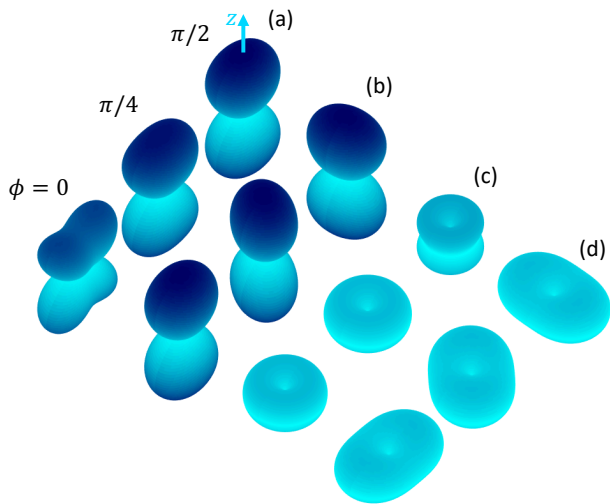


FIG. 4. PADs as defined in eqs. (12)–(19) for geometries (a)–(d), respectively, but normalized to  $\sigma = 1$  for IR field phase  $\phi = 0, \pi/4, \pi/2$  for the sideband at  $\approx 9.5$  eV.

### III. NUMERICAL CALCULATIONS AND DISCUSSION

In this part, the results of calculations of photoionization probability and angular anisotropy parameters in neon valance shell ionization by the pulse consisting of IR with  $\omega = 1.55$  eV and its 17th, 19th and 21nd harmonics are presented. The electric field parameters were set to the values typical for RABBITT experiments:  $E_{\text{xuv}}^0 = 10^{-4}$  a.u.,  $E_{\text{ir}}^0 = 2.5 \cdot 10^{-3}$  a.u., and  $\tau = 10$  fs. Note that according to eq. (1), duration of XUV components is twice shorter than one of IR component.

Reduced dipole matrix elements between ground state  $2s^2 2p^6 1S$  and continuum states  $2s^2 2p^5 \epsilon l^1 L$  were calculated in MCHF package [48] with non-orthogonal  $2p$  orbital. For the ground state, the experimental ionization energy was used. Reduced dipole matrix elements between continuum states were calculated using a method described in [49] involving angular momentum algebra [46] to convert the radial integrals to the matrix elements in an appropriate angular momentum coupling scheme.

In figure 3, there are dimensionless parameters  $\beta_{kq}$  defined by eqs. (12)–(19) calculated by both RE and PT methods plotted together with integrated spectrum. Here we set all  $\phi_N$  to zero. The central peak is mainline caused by 19th harmonic, two lower lines on the sides of ML19 are sidebands SB18 and SB20. For (a)- and (c)-geometry, calculations at three phases  $\phi = 0, \pi/4$  and  $\pi/2$  of the IR component are presented. For (b) and (d)-geometry, presented parameters do not depend on IR phase. For the (a)-geometry at  $\phi = 0$  and for (c)-geometry at  $\phi = \pi/2$ , the integrated probability is negligible, therefore dimensionless anisotropy parameters are much less trustworthy and are not presented. The overall agreement between the methods is good. As RE calculation is more rugged, it is shown partly where it

is necessary for discussion and do not interfere the total readability.

The angular anisotropy parameters vary smoothly through the lines except the edges where photoemission probability drops down. As it is clear from equations (15) and (19),  $\beta_{22(42)}$  are responsible for the PADs' dependency on azimuth angle, while  $\beta_{2(4)}$  are responsible for axially symmetrical contribution. In all the cases, parameters  $\beta_{22}$  are much smaller than  $\beta_2$  and compatible with  $\beta_4$  and  $\beta_{42}$ . The minor value of these parameters is a result of interference between the ionization to  $f$ - and  $p$ -wave.

For the geometries (a)–(c), if only  $f$ -wave is important due to a spectroscopic feature, the anisotropy parameters tend to  $\beta_2 \rightarrow 4/7$ ,  $\beta_4 \rightarrow -4/7$ ,  $\beta_{22} \rightarrow -2\sqrt{6}/7$  (if exists) and  $\beta_{42} \rightarrow -\sqrt{10}/7$  (if exists).

As it was already mentioned, in the (a) and (c) geometries, the spectrum as well as parameters  $\beta_{kq}$  depend on the IR phase  $\phi$  (see panels (a) and (c) in figure 3). For the (a)- and (c)-geometry, formal equations for the integrated spectrum and  $\beta_4$  in terms of dynamical parameters (11) coincide. Nevertheless, one should remember that the corresponding amplitudes depend on IR phase, and the last being written in form of eq. (1) possesses a different physical meaning for different geometries. The easiest way to illustrate is that  $\phi = 0$  means  $\mathbf{E}_{\text{xuv}} \parallel z$  and  $\mathbf{E}_{\text{ir}} \parallel x$  for (a)-geometry, while  $\phi = 0$  means  $\mathbf{E}_{\text{xuv}} \parallel x$  and  $\mathbf{E}_{\text{ir}} \parallel y$  for (c)-geometry. Therefore, the same values of observables are reached at different phases. The difference in  $\beta_2$  originates from different signs before the interference terms  $B^{\nu\mu}[1, 2]$  (see factor  $(-1)^{L+L'+1}$  in eq. (12)). If for some reason either  $L = 1$  ( $P$ -term) or  $L = 2$  ( $D$ -term) dominates,  $\beta_2$  in these geometries would also coincide.

In figure 4, the calculated PADs for different geometries and IR phases are presented. In the schemes (a) and (b),  $\beta_2$  is positive, therefore, the maximum photoelectron emission is found along the quantization axis ( $\theta = 0, \pi$ ) because the other  $\beta$ s are much smaller.  $\beta_2$  is also positive when both of the field components are linearly polarized in the same direction [25, 47]. In the schemes (c) and (d),  $\beta_2$  is negative, therefore, the maximum photoelectron emission is found in the plane perpendicular to the quantization axis ( $\theta = \pi/2$ ). The PADs keep their form for the phases corresponding essential signals in the sidebands and diverge for the phases corresponding a minor sidebands ( $\phi = 0$  for (a)- and  $\phi = \pi/2$  for (c)-geometry) they become quite diverse: as  $\beta_2$  sharply changes (its absolute values decrease, similar to fig. 5),  $Y_{4,22,42}(\theta, \varphi)$  play a more significant role (see fig. 4a,c). For these phases, PADs resemble the ones for helium-like case (fig. 2a,c). In schemes (b) and (d), as it was previously mentioned, PAD rotates around  $z$ -axis, with variation of the IR component phase  $\phi$ . For neon the effect of rotation is more prominent for the geometry (d) (see fig. 4b,d).

Until now, we assumed that all of the XUV harmonics phases are zero  $\phi_N = 0$ . In order to investigate the role of the XUV phases, we chose (c)-geometry (see fig. 5)

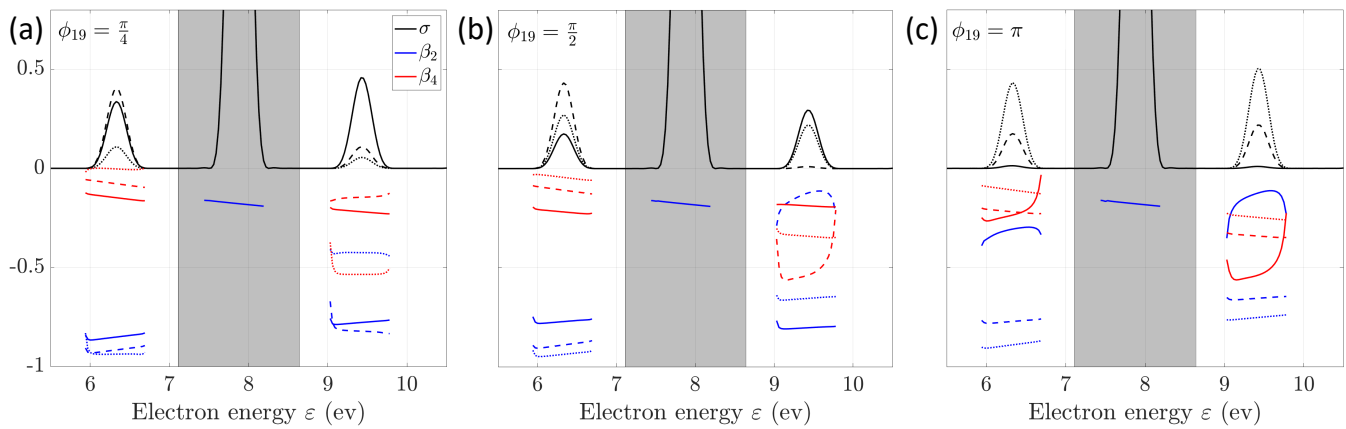


FIG. 5. PT calculations as in figure 3c, but for different phases of 19th harmonic.

and assigned several different values to  $\phi_{19}$ . One can see that varying the phase of an XUV component leads to the rearrangement of the photoemission signal therefore the same magnitudes are achieved at different IR phases. The range of variation for the anisotropy parameters remains the same as well.

#### IV. CONCLUSION

In the paper we investigated how the polarization and propagation direction of the field's components affect kinematic of photoionization in the RABBITT scheme. We considered: (a) crossed linearly polarized IR and XUV harmonics; (b,c) either XUV or IR is linearly polarized and the remaining component is circularly polarized (d) both IR and XUV are circularly polarized.

Among the considered geometries, the setup with circularly polarized XUV harmonics and linearly polarized IR component possesses the highest symmetry (axial). This geometry as well as setup with crossed linearly polarized components, allows for the observation of RABBITT oscillations in both angle-integrated and angle-resolved probabilities of electron emission.

On the contrary, for a circularly polarized IR field and either linearly or circularly polarized XUV harmonics, there is only one symmetry plane, and RABBITT oscillations are observed only in the angular distribution of photoemission. In these geometries, the variation of the IR phase appears as a rotation of PAD with respect to axis oriented along the direction of IR component prop-

agation.

To distinguish between geometrical (inherited solely from the polarization of the electromagnetic field) and spectroscopic (inherited from the properties of the target, and thus dependent on photon energies) features, we considered neon and helium-like targets. In the first case, the observable values are determined by the interplay between different ionization channels, whereas for helium, the system may reduce to completely geometrical, with a PAD that does not depend on dynamic parameters, such as photon energy or even specific atom.

For circularly polarized XUV comb, the symmetries are the same for both multichannel targets and helium-like ones. In geometries with linearly polarized XUV component, there are two additional symmetry planes for helium-like targets, moreover, for linearly polarized IR component, they are geometrical and make angle  $\pm\pi/4$  with polarization vector, while for circularly polarized IR component, they are dynamical and depend on phase between up- and down-transitions.

#### ACKNOWLEDGMENTS

The part of research related to the general approach (section II) was funded by the Russian Science Foundation (RSF) under project No. 22-12-00389 and the numerical simulations were supported Ministry of Science and Higher Education of the Russian Federation grant No. 075-15-2021-1353.

[1] U. Becker and D. A. Shirley, eds., *VUV and Soft X-Ray Photoionization* (Plenum Press, New York and London, 1996).

[2] F. J. Wuilleumier and M. Meyer, Pump-probe experiments in atoms involving laser and synchrotron radi-

ation: an overview, *Journal of Physics B: Atomic, Molecular and Optical Physics* **39**, R425 (2006).

[3] R. Mitzner, A. A. Sorokin, B. Siemer, S. Roling, M. Rutkowski, H. Zacharias, M. Neeb, T. Noll, F. Siewert, W. Eberhardt, M. Richter, P. Juranic, K. Tiedtke,

- and J. Feldhaus, Direct autocorrelation of soft-x-ray free-electron-laser pulses by time-resolved two-photon double ionization of He, *Phys. Rev. A* **80**, 025402 (2009).
- [4] P. Radcliffe, S. Düterer, A. Azima, H. Redlin, J. Feldhaus, J. Dardis, K. Kavanagh, H. Luna, J. P. Gutierrez, P. Yeates, E. T. Kennedy, J. T. Costello, A. Delsierieys, C. L. S. Lewis, R. Taïeb, A. Maquet, D. Cubaynes, and M. Meyer, Single-shot characterization of independent femtosecond extreme ultraviolet free electron and infrared laser pulses, *Applied Physics Letters* **90**, 131108 (2007).
- [5] M. Lewenstein, P. Balcou, M. Y. Ivanov, A. L'Huillier, and P. B. Corkum, Theory of high-harmonic generation by low-frequency laser fields, *Phys. Rev. A* **49**, 2117 (1994).
- [6] G. Sansone, E. Benedetti, F. Calegari, C. Vozzi, L. Avaldi, R. Flammini, L. Poletto, P. Villoresi, C. Altucci, R. Velotta, S. Stagira, S. D. Silvestri, and M. Nisoli, Isolated single-cycle attosecond pulses, *Science* **314**, 443 (2006), <https://www.science.org/doi/pdf/10.1126/science.1132838>.
- [7] V. V. Strelkov, V. T. Platonenko, A. F. Sterzhantov, and M. Y. Ryabikin, Attosecond electromagnetic pulses: generation, measurement, and application. generation of high-order harmonics of an intense laser field for attosecond pulse production, *Physics-Uspekhi* **59**, 425 (2016).
- [8] K. C. Prince, E. Allaria, C. Callegari, R. Cucini, G. D. Ninno, and S. D. M. et al, Coherent control with a short-wavelength free-electron laser, *Nat. Photonics* **10**, 176 (2016).
- [9] C. Callegari, A. N. Grum-Grzhimailo, K. L. Ishikawa, K. C. Prince, G. Sansone, and K. Ueda, Atomic, molecular and optical physics applications of longitudinally coherent and narrow bandwidth free-electron lasers, *Physics Reports* **904**, 1 (2021), atomic, molecular and optical physics applications of longitudinally coherent and narrow bandwidth Free-Electron Lasers.
- [10] F. Krausz and M. Ivanov, Attosecond physics, *Rev. Mod. Phys.* **81**, 163 (2009).
- [11] R. Pazourek, S. Nagele, and J. Burgdörfer, Time-resolved photoemission on the attosecond scale: opportunities and challenges, *Faraday Discuss.* **163**, 353 (2013).
- [12] J. Vos, L. Cattaneo, S. Patchkovskii, T. Zimmermann, C. Cirelli, M. Lucchini, A. Kheifets, A. S. Landsman, and U. Keller, Orientation-dependent stereo wigner time delay and electron localization in a small molecule, *Science* **360**, 1326 (2018), <https://www.science.org/doi/pdf/10.1126/science.aao4731>.
- [13] M. Ossiander, J. Riemensberger, S. Neppl, M. Mittermair, M. Schaffer, A. Duensing, M. S. Wagner, R. Heider, M. Wurzer, M. Gerl, and et al, Absolute timing of the photoelectric effect, *Nature* **561**, 374 (2018).
- [14] V. Véliard, R. Taïeb, and A. Maquet, Phase dependence of  $(n + 1)$ -color ( $n > 1$ ) ir-uv photoionization of atoms with higher harmonics, *Phys. Rev. A* **54**, 721 (1996).
- [15] P. M. Paul, E. S. Toma, P. Breger, G. Mullot, F. Augé, P. Balcou, H. G. Muller, and P. Agostini, Observation of a train of attosecond pulses from high harmonic generation, *Science* **292**, 1689 (2001), <https://www.science.org/doi/pdf/10.1126/science.1059413>.
- [16] H. Muller, Reconstruction of attosecond harmonic beating by interference of two-photon transitions, *Appl. Phys. B* **74**, 17 (2002).
- [17] Y. Mairesse, A. de Bohan, L. J. Frasinski, H. Merdji, L. C. Dimu, P. Monchicourt, P. Breger, M. Kovačev, R. Taïeb, B. Carrè, H. G. Muller, P. Agostini, and P. Salières, Attosecond synchronization of high-harmonic soft x-rays, *Science* **302**, 1540 (2003), <https://www.science.org/doi/pdf/10.1126/science.1090277>.
- [18] J. Dahlström, A. L'Huillier, and A. Maquet, Introduction to attosecond delays in photoionization, *J. Phys. B: At. Mol. Opt. Phys.* **45** (2012).
- [19] J. Dahlström, D. Guènot, K. Klünder, M. Gisselbrecht, J. Mauritsson, A. L'Huillier, A. Maquet, and R. Taïeb, Theory of attosecond delays in laser-assisted photoionization, *Chemical Physics* **414**, 53 (2013).
- [20] A. Harth, N. Douguet, K. Bartschat, R. Moshhammer, and T. Pfeifer, Extracting phase information on continuum-continuum couplings, *Phys. Rev. A* **99**, 023410 (2019).
- [21] A. S. Kheifets and A. W. Bray, RABBITT phase transition across the ionization threshold, *Phys. Rev. A* **103**, L011101 (2021).
- [22] G. Laurent, W. Cao, H. Li, Z. Wang, I. Ben-Itzhak, and C. L. Cocke, Attosecond control of orbital parity mix interferences and the relative phase of even and odd harmonics in an attosecond pulse train, *Phys. Rev. Lett.* **109**, 083001 (2012).
- [23] S. A. Aseyev, Y. Ni, L. J. Frasinski, H. G. Muller, and M. J. J. Vrakking, Attosecond angle-resolved photoelectron spectroscopy, *Phys. Rev. Lett.* **91**, 223902 (2003).
- [24] D. Villeneuve, P. Hockett, M. Vrakking, and H. Niikura, Coherent imaging of an attosecond electron wave packet, *Science* **356**, 1150 (2017).
- [25] J. Joseph, F. Holzmeier, D. Bresteau, C. Spezzani, T. Ruchon, J. F. Hergott, O. Tcherbakoff, P. D. Oliveira, J. C. Houver, and D. Doweck, Angle-resolved studies of XUV - IR two-photon ionization in the RABBITT scheme, *Journal of Physics B: Atomic, Molecular and Optical Physics* **53**, 184007 (2020).
- [26] C. Cirelli, C. Marante, S. Heuser, C. L. M. Petersson, A. J. Galan, L. Argenti, D. B. S. Zhong, M. Isinger, S. Nandi, and et al., Anisotropic photoemission time delays close to a fano resonance, *Nature Comm.* **9**, 955 (2018).
- [27] W. Jiang, G. Armstrong, J. Tong, and et al., Atomic partial wave meter by attosecond coincidence metrology., *Nat Commun* **13**, 5072 (2022).
- [28] A. S. Kheifets and Z. Xu, Polarization control of RABBITT in noble gas atoms, *Journal of Physics B: Atomic, Molecular and Optical Physics* **56**, 155601 (2023).
- [29] S. Heuser, G. A. Jiménez, C. Cirelli, C. Marante, M. Sabbar, R. Boge, M. Lucchini, L. Gallmann, I. Ivanov, A. S. Kheifets, J. M. Dahlström, E. Lindroth, L. Argenti, F. Martín, and U. Keller, Angular dependence of photoemission time delay in helium, *Phys. Rev. A* **94**, 063409 (2016).
- [30] G. Laurent, W. Cao, H. Li, Z. Wang, I. Ben-Itzhak, and C. L. Cocke, Attosecond control of orbital parity mix interferences and the relative phase of even and odd harmonics in an attosecond pulse train, *Phys. Rev. Lett.* **109**, 083001 (2012).
- [31] P. Hockett, Angle-resolved RABBITT: theory and numerics, *Journal of Physics B: Atomic, Molecular and Optical Physics* **50**, 154002 (2017).
- [32] D. Busto, J. Vinbladh, S. Zhong, M. Isinger, S. Nandi, S. Maclot, P. Johnsson, M. Gisselbrecht, A. L'Huillier, E. Lindroth, and J. M. Dahlström, Fano's propensity

- rule in angle-resolved attosecond pump-probe photoionization, *Phys. Rev. Lett.* **123**, 133201 (2019).
- [33] J. Fuchs, N. Douguet, S. Donsa, F. Martin, J. Burgdörfer, L. Argenti, L. Cattaneo, and U. Keller, Time delays from one-photon transitions in the continuum, *Optica* **7**, 154 (2020).
- [34] D. Bharti, H. Srinivas, F. Shobeiry, K. R. Hamilton, R. Moshhammer, T. Pfeifer, K. Bartschat, and A. Harth, Multisideband interference structures observed via high-order photon-induced continuum-continuum transitions in argon, *Phys. Rev. A* **107**, 022801 (2023).
- [35] J. Peschel, P. Busto, D., and M. et al., Attosecond dynamics of multi-channel single photon ionization, *Nat Commun* **13**, 5205 (2022).
- [36] A. N. Grum-Grzhimailo, S. Fritzsche, P. O’Keeffe, and M. Meyer, Universal scaling of resonances in vector correlation photoionization parameters, *J. Phys. B: At. Mol. Opt. Phys* **38**, 2545 (2005).
- [37] P. K. Maroju, C. Grazioli, M. D. Fraia, M. Moioli, D. Ertel, H. Ahmadi, O. Plekan, P. Finetti, E. Allaria, L. Giannessi, G. D. Ninno, S. Spampinati, A. A. Lutman, R. J. Squibb, R. Feifel, P. Carpeggiani, M. Reduzzi, T. Mazza, M. Meyer, S. Bengtsson, N. Ibrakovic, E. R. Simpson, J. Mauritsson, T. Csizmadia, M. Dumergue, S. Kühn, N. G. Harshitha, D. You, K. Ueda, M. Labeye, J. E. Bækhoj, K. J. Schafer, E. V. Gryzlova, A. N. Grum-Grzhimailo, K. C. Prince, C. Callegari, and G. Sansone, Attosecond pulse shaping using a seeded free-electron laser, *Nature* **578**, 386–391 (2020).
- [38] P. K. Maroju, C. Grazioli, M. D. Fraia, M. Moioli, D. Ertel, H. Ahmadi, O. Plekan, P. Finetti, E. Allaria, L. Giannessi, G. D. Ninno, S. Spampinati, A. A. Lutman, R. J. Squibb, R. Feifel, P. Carpeggiani, M. Reduzzi, T. Mazza, M. Meyer, S. Bengtsson, N. Ibrakovic, E. R. Simpson, J. Mauritsson, T. Csizmadia, M. Dumergue, S. Kühn, N. G. Harshitha, D. You, K. Ueda, M. Labeye, J. E. Bækhoj, K. J. Schafer, E. V. Gryzlova, A. N. Grum-Grzhimailo, K. C. Prince, C. Callegari, and G. Sansone, Analysis of two-color photoelectron spectroscopy for attosecond metrology at seeded free-electron lasers, *New Journal of Physics* **23**, 043046 (2021).
- [39] P. K. Maroju, C. Grazioli, M. Di Fraia, M. Moioli, D. Ertel, H. Ahmadi, O. Plekan, P. Finetti, E. Allaria, L. Giannessi, G. De Ninno, A. A. Lutman, R. J. Squibb, R. Feifel, P. Carpeggiani, M. Reduzzi, T. Mazza, M. Meyer, S. Bengtsson, N. Ibrakovic, E. R. Simpson, J. Mauritsson, T. Csizmadia, M. Dumergue, S. Kühn, H. N. Gopalakrishnan, D. You, K. Ueda, M. Labeye, J. E. Bækhoj, K. J. Schafer, E. V. Gryzlova, A. N. Grum-Grzhimailo, K. C. Prince, C. Callegari, and G. Sansone, Complex attosecond waveform synthesis at fel fermi, *Applied Sciences* **11** (2021).
- [40] D. I. R. Boll and O. A. Fojón, Attosecond polarization control in atomic RABBITT-like experiments assisted by a circularly polarized laser, *J. Phys. B* **50** (2017).
- [41] Y. Liao, E. Olofsson, J. M. Dahlström, L.-W. Pi, Y. Zhou, and P. Lu, Circularly polarized rabbitt applied to a rabi-cycling atom, *Phys. Rev. A* **109**, 043104 (2024).
- [42] A. Fleischer, O. Kfir, T. Diskin, P. Sidorenko, and O. Cohen, Spin angular momentum and tunable polarization in high-harmonic generation, *Nature Photon.* **8**, 543–549 (2014).
- [43] M. Ivanov and E. Pisanty, Taking control of polarization, *Nature Photonics* **8**, 501–503 (2014).
- [44] M. Han, J. Ji, T. Balčiūnas, and et al., Attosecond circular-dichroism chronoscopy of electron vortices., *Nat. Phys.* **19**, 230–236 (2023).
- [45] T. S. Sarantseva, A. A. Romanov, A. A. Silaev, N. V. Vvedenskii, and M. V. Frolov, High-order harmonic generation in orthogonal ir and xuv pulses: Xuv-initiated channel separation and polarization control, *Phys. Rev. A* **107**, 023113 (2023).
- [46] M. Popova, S. Yudin, E. Gryzlova, M. Kiselev, and A. Grum-Grzhimailo, Attosecond interferometry involving discrete states, *Journal of Experimental and Theoretical Physics* **136**, 259 (2023).
- [47] S. Yudin, M. Popova, M. Kiselev, S. Burkov, E. Gryzlova, and A. Grum-Grzhimailo, Attosecond interferometry of neon atom: Photoelectron angular distributions, *Moscow University Physics Bulletin* **78**, 347 (2023).
- [48] C. Froese Fischer, T. Brage, and P. Jönsson, *Computational Atomic Structure. An MCHF Approach* (Bristol, Institute of Physics Publishing, 1997).
- [49] T. Mercouris, Y. Komninos, S. Dionissopoulou, and C. A. Nicolaides, Effects on observables of the singularity in the multiphoton free - free dipole matrix elements, *Journal of Physics B: Atomic, Molecular and Optical Physics* **29**, L13 (1996).